ACS OMEGA

http://pubs.acs.org/journal/acsodf

Article

Intrinsic Enzyme-like Activities of Cerium Oxide Nanocomposite and Its Application for Extracellular H_2O_2 Detection Using an Electrochemical Microfluidic Device

Negar Alizadeh, Abdollah Salimi,* Tsun-Kong Sham, Paul Bazylewski, and Giovanni Fanchini

Cite This: *ACS Omega* 2020, 5, 11883−11894

Read Online

ACCESS | Metrics & More | Article Recommendations

ABSTRACT: Artificial enzyme mimics have gained considerable attention for use in sensing applications due to their high stability and outstanding catalytic activity. We show that cerium oxide nanosheets (NSs) exhibit triple-enzyme mimetic activity. The oxidase-, peroxidase-, and catalase-like activities of the proposed nanoparticles are demonstrated using both colorimetric and electron paramagnetic resonance (EPR) spectroscopy. On the basis of the excellent catalytic activity of cerium oxide NSs toward hydrogen peroxide, an electrochemical approach for the high-throughput detection of H_2O_2 in living cells was established. This report presents an analytical microfluidic chip integrated with a cerium oxide NS mimic enzyme for the fabrication of a simple, sensitive, and low-cost electrochemical sensor. Three Au microelectrodes were fabricated on a glass substrate using photolithography, and the working electrode was functionalized using cerium oxide NSs. The operation of this biosensor is based on cerium oxide NSs and presents a high sensitivity over a wide detection range, between 100 nM and 20 mM, with a low detection limit of 20 nM and a high sensitivity threshold of 226.4 $\mu A \cdot cm^{-2} \cdot \mu M^{-1}$. This microfluidic sensor shows a strong response to H_2O_2, suggesting potential applications in monitoring H_2O_2 directly secreted from living cells. This sensor chip provides a promising platform for applications in the field of diagnostics and sensing.

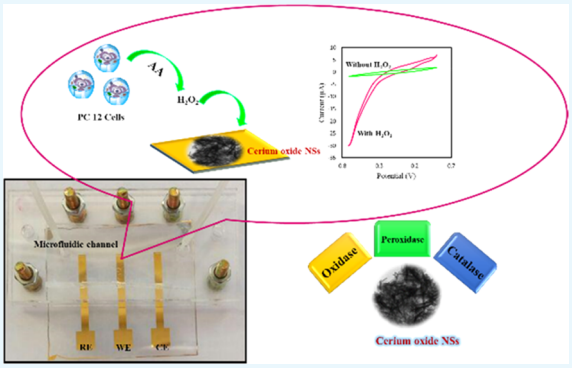

1. INTRODUCTION

Since the first exciting discovery of ferromagnetic nanoparticles,[1] various efficient nanomaterial-based mimic enzymes (nanozymes)[2] have been developed over the past few decades. Such nanomaterials can catalyze specific redox-like-type reactions and exhibit great activity for oxidase-like,[3,4] peroxidase-like,[5−7] catalase-like,[8,9] or superoxide dismutase-like (SOD) reactions.[10,11] To date, there have been numerous works devoted to exploring nanomaterials' enzyme mimetics from carbon- and metal-based nanomaterials.[12,13] Recently, metal nanomaterials have become an area of increasing interest because of unique electronic and a larger variety of enzyme-like characteristics.[14,15] These nanozymes are widely used in sensing and diagnosis applications.[16] For example, Wang et al. developed a direct electrochemical assay for kanamycin detection based on the peroxidase-like activity of gold nanoparticles.[17] AuNPs could catalyze the reaction between H_2O_2 and reduced thionine to produce oxidized thionine. This reaction exhibited a distinct reduction peak on gold electrode in differential pulse voltammetry (DPV) and could be utilized to quantify the concentration of kanamycin. Furthermore, Wang and his colleagues fabricated FePt−Au ternary metallic nanoparticles with powerful enzymatic mimic for H_2O_2 sensing.[15] Among nanozymes, multiactivity nanozymes with two or more catalytic activities have attracted significant attention.[18,19] Some nanozymes such as Co_3O_4,[20] Ni−Pd NPs,[21] CoMo hybrids,[22] and V_6O_{13}[23] have been reported with two or more catalytic activities. These kinds of nanozymes can have more effective applications in physiological and pathological processes.

Cerium oxide nanoparticles (nanoceria) have attracted enormous interest in recent years as nanocatalysts due to their unique physical and chemical properties. Nanoceria has been widely applied in various fields, such as catalysis, bioassays, and antioxidant therapy.[24,25] This rare-earth oxide nanostructure shows high catalytic performance in various applications due to the presence of mixed valence states of Ce^{3+} and Ce^{4+}, and the presence of oxygen vacancies. The key to this catalytic activity is that the redox couple can switch

Received: October 2, 2019
Accepted: March 23, 2020
Published: May 19, 2020

https://dx.doi.org/10.1021/acsomega.9b03252
ACS Omega 2020, 5, 11883−11894

Scheme 1. (A) Mimicking Three Different Enzymes Peroxidase, Catalase, and Oxidase by Individual Material Cerium Oxide, (B) Schematic Representation and Photograph of Lab-on-a-Chip Setup for the Electrocatalytic Reduction of H_2O_2

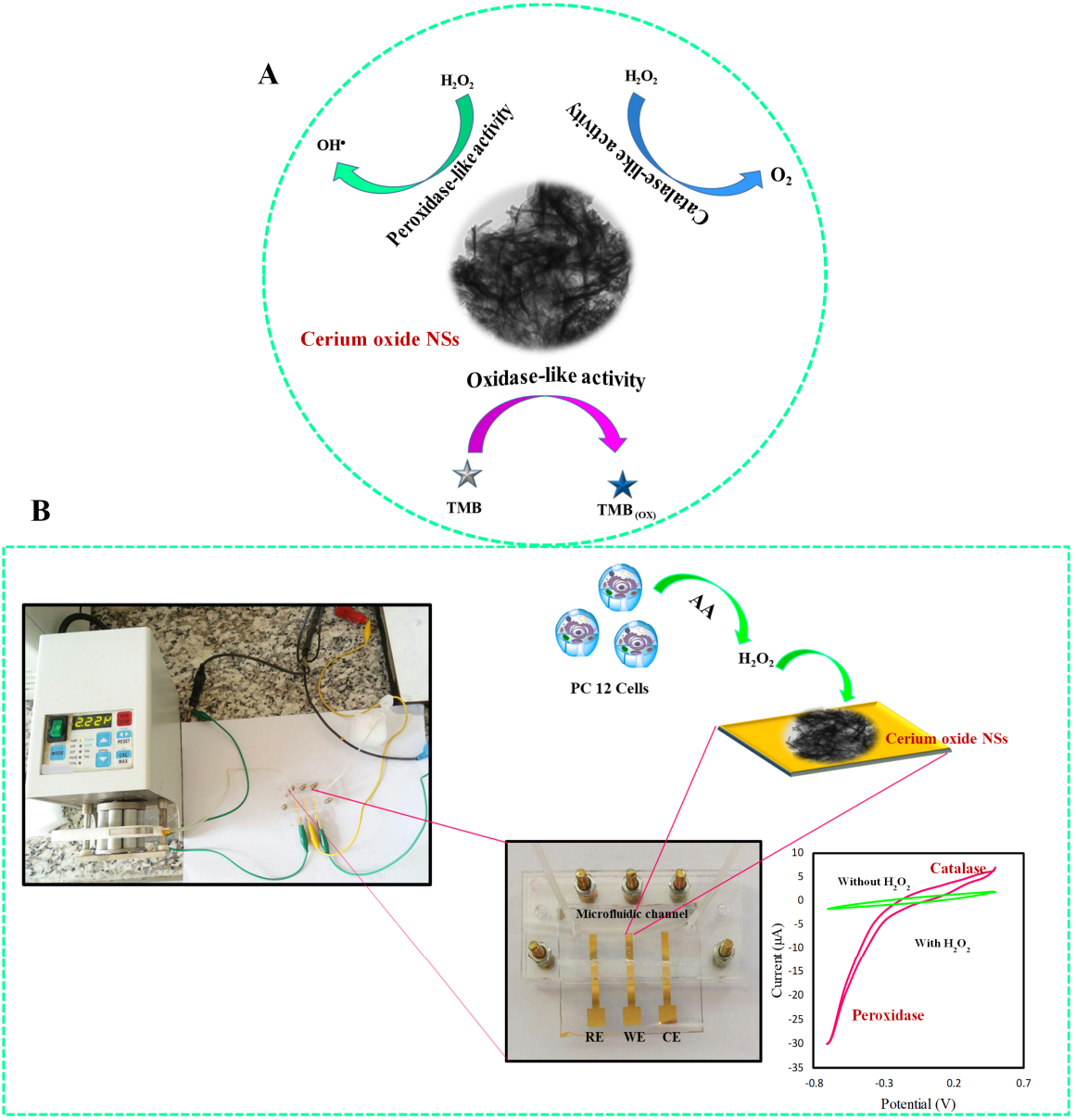

between each state in a $CeO_2 \leftrightarrow CeO_{2-x} + x/2O_2$ ($Ce^{4+} \leftrightarrow Ce^{3+}$) recycle process.[26,27] The catalytic activity of nanoceria originates from the surface oxygen; thus, the active oxygen content on the surface must be increased to improve catalytic activities. As a result, increasing the $Ce^{3+}/(Ce^{3+} + Ce^{4+})$ ratio (shorted as "Ce^{3+} ratio") enhances the surface oxygen defect in the structure, leading to improvement in catalytic properties.[28,29]

It is worth noting that H_2O_2 has a considerable impact on food production, textile industry, paper bleaching, pharmaceutical research, and environment pollution.[30,31] It is a byproduct of various enzymatic reactions including glucose oxidase, cholesterol oxidase, glutamate oxidase, urate oxidase, lactate oxidase, alcohol oxidase, lysine oxidase, oxalate oxidase, and horseradish peroxidase.[32] In living organisms, H_2O_2 regulates diverse biological processes such as immune cell activation, vascular remodeling, apoptosis, and root growth. The presence of excess H_2O_2 in living organisms also causes severe diseases like cancer and Parkinson's disease.[33,34] The determination of H_2O_2 in biological environments is of critical importance. Electrochemical methods have attracted great interest over competing H_2O_2 detection techniques such as chromatography,[35] chemiluminescence,[36] colorimetry,[37] and fluorescence,[38] due to their high sensitivity, fast response, low cost, and convenient operation.[39,40]

The microfluidic lab-on-a-chip (LOC) technology is recognized as one of the most promising tools to develop novel diagnostic platforms.[41] Microfluidic chips can be applied as point-of-care (POC) devices for clinical diagnostics because of their inherent small size, portability, low cost, easy operation, and low amount of biological sample required.[42,43] These devices include a set of microfluidic channels to control fluid flow throughout the chip, in which various procedures such as reagent mixing, affinity-based binding, and signal transduction can be implemented side-by-side.[44] Sensors can be integrated within microfluidic devices to enable continuous

https://dx.doi.org/10.1021/acsomega.9b03252
ACS Omega 2020, 5, 11883−11894

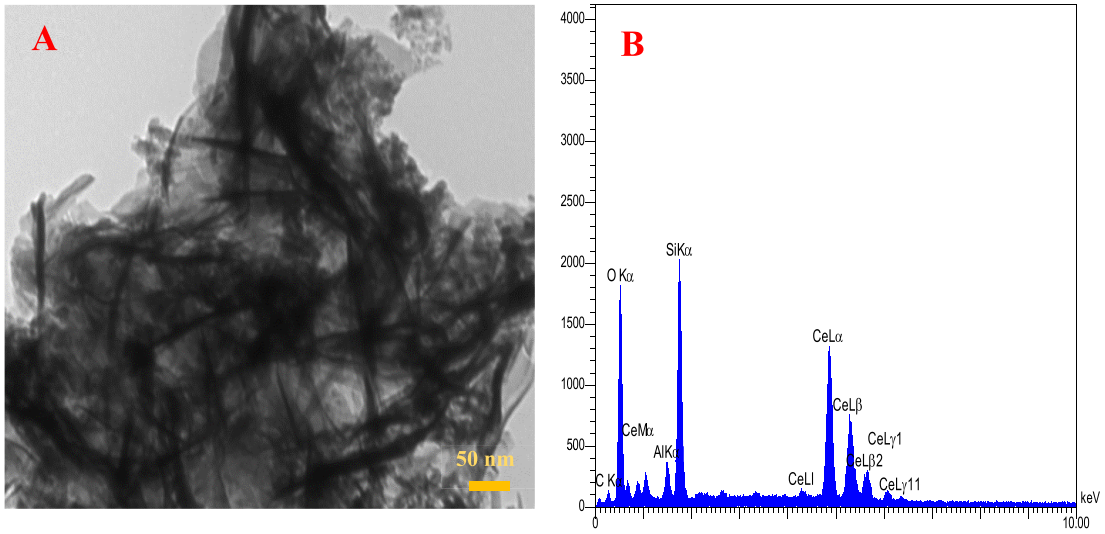

Figure 1. (A) TEM image and (B) EDS spectra of cerium oxide NSs.

measurement of single or multiple analytes in small sample volumes.[45]

In this work, we present a microfluidic electrochemical LOC for the real-time detection of H_2O_2 using a cerium oxide nanosheet (NS)-modified Au working electrode. Cerium oxide NSs were synthesized via a simple hydrothermal route, and they simultaneously displayed oxidase-, peroxidase-, and catalase enzyme-like activities (Scheme 1). Cerium oxide NSs were integrated with a microfluidic platform for the effective detection of H_2O_2. This sensor is found to be highly selective and specific toward H_2O_2 with negligible interference from analytes such as glucose, dopamine, uric acid, glutathione, and ascorbic acid. Furthermore, cerium oxide NS-based LOC devices can find practical use in monitoring H_2O_2 inside living cells, which is indicative of their viability in real-world analysis applications.

2. RESULTS AND DISCUSSION

2.1. Structure Characterization of Prepared Cerium Oxide. The morphology of cerium oxide was investigated by transmission electron microscopy (TEM). Figure 1A shows the wrinkled nanosheet structure of the prepared cerium oxide, which shows a large surface area for the reaction with H_2O_2. The energy-dispersive spectrometry (EDS) analysis of cerium oxide NSs revealed their elemental composition and corroborated the presence of Ce, C, and O in these nanostructures (Figure 1B).

Figure 2A shows the X-ray diffraction (XRD) patterns of cerium oxide NSs. The XRD peaks are located at angles (2θ) of 28.6, 32.84, 47.27, 55.83, 59.09, 69.02, 76.74, and 78.64°, corresponding to the (111), (200), (220), (311), (222), (400), (331), and (420) planes of CeO_2 in the face-centered cubic phase (JCPDS data card no: 34-0394).[46] Peaks at angles 2θ = 44.12 and 64.42° can be assigned to $Ce_2O(CO_3)_2{\cdot}H_2O$.[47] The formation of $Ce_2O(CO_3)_2{\cdot}H_2O$ is due to the reaction of the Ce^{3+} ions from cerium nitrate hexahydrate with the CO_3^{2-} and OH^- ions from the hydrolysis of urea and terephthalic acid.[48] $Ce_2O(CO_3)_2{\cdot}H_2O$ improves the $Ce^{3+}/(Ce^{3+} + Ce^{4+})$ ratio in the structure and promotes the formation of oxygen vacancy. Significantly, oxygen vacancies enhance the redox ability and allow easier surface reaction, which is in favor of catalytic reaction.[29] The thermal stability of cerium oxide NSs was investigated through thermogravimetric analysis (TGA). As can be seen from Figure 2B, weight loss occurs by the following three steps: (1) release of physically adsorbed water, with 7.9% weight loss from room temperature to 160 °C; (2) decomposition of cerium carbonate to form ceria, with 12.0% weight loss from 160 to 470 °C, which is representative of the surface $Ce^{3+}/(Ce^{3+} + Ce^{4+})$ ratio; and (3) minimum weight loss above 470 °C, which can be attributed to the removal of captured CO_2.[49] Figure 2C shows the Fourier transform infrared (FTIR) spectra of urea, terephthalic acid, and cerium oxide NSs. Urea has characteristic vibrational peaks at 3348 and 3443 cm^{-1} (NH_2 group stretching) and at 1680 cm^{-1} (−C═O group stretching) (curve a).[50] Peaks from terephthalic acid, at 2542, 1682, and 1570−1424 cm^{-1}, are assigned to −COOH, −C═O, and an aromatic ring of the terephthalic acid, respectively. Concerning the IR spectrum of terephthalic acid (curve b) peaks in the 1285−1000 cm^{-1} region are fingerprints of −C−OH, −C═O, −C−CH, and −C−H bending modes, while the 700−800 cm^{-1} region contains the terephthalic acid aromatic ring bending mode.[51] The IR spectrum of cerium oxide NSs (curve c) is different from its counterpart from reagents, in which most of the IR peaks are not present. Specifically, the broad IR absorption band 3422 cm^{-1} in the spectra of cerium oxide NSs is assigned to O−H stretching modes from residual water and Ce−OH, which is present in nanostructured cerium oxide because of its higher surface-to-volume ratio. Likewise, the same effect may be responsible for the absorption peak observed at 1019 cm^{-1}, which can be attributed to C−O−Ce and is also not present in bulk cerium oxide.

2.2. Triple-Enzyme Catalytic Activity of Cerium Oxide NSs. To investigate the triple-enzyme catalytic activity of cerium oxide NSs and their oxidase-, peroxidase-, and catalase-like activities, a series of experiments were carried out as indicated in the following subsections.

2.2.1. Peroxidase-like Catalytic Activity of Cerium Oxide NSs. The peroxidase-like catalytic activity of cerium oxide NSs was investigated by catalyzing the oxidation of 3,3′,5,5 tetramethylbenzidine (TMB) in the presence of H_2O_2. As shown by curve a in Figure 3A, as-synthesized cerium oxide NSs show strong optoelectronic absorption in the visible region between 395 and 420 nm. After the addition of cerium

https://dx.doi.org/10.1021/acsomega.9b03252
ACS Omega 2020, 5, 11883−11894

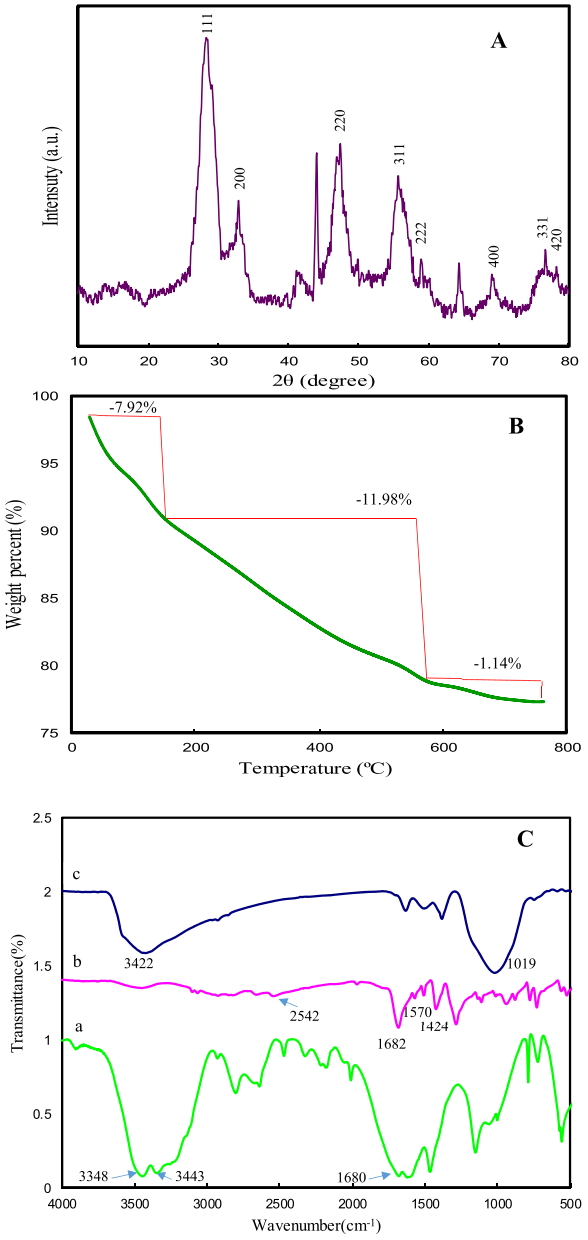

Figure 2. (A) XRD patterns. (B) TGA analysis. (C) FTIR spectra of (a) urea, (b) terephthalic acid, and (c) cerium oxide NSs.

oxide NSs to an aqueous solution of TMB + H_2O_2, an additional strong adsorption peak at 652 nm is observed, and the color of the solution turned blue (Figure 3A, curve b). After adding H_2SO_4, the adsorption peak at 652 nm disappears with the appearance of a peak at 450 nm and the color of the solution changed from blue to yellow (Figure 3A, curve c).

The oxidation reaction was catalyzed by peroxidase, but the catalytic activity of cerium oxide could be stopped by H_2SO_4, leading to the cation radical of the TMB molecule, which further lost another electron to form diamine.[52] These changes could be expressed as follows

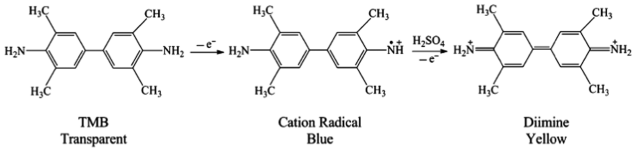

No color change was observed in the absence of cerium oxide NSs. This clearly shows that cerium oxide NSs showed peroxidase-like catalytic activity. Steady-state kinetic experiments were performed to further investigate the peroxidase-like catalytic property of cerium oxide NSs. As displayed in Figure 4, the initial rate versus TMB and H_2O_2 concentrations both followed with typical Michaelis−Menten behaviors in a certain range of substrate concentration. The Michaelis−Menten constant (K_m) and maximum initial velocity (V_{max}) were calculated using the Lineweaver−Burk plot (inserted Figure 4). It is known that the lower K_m value reflects a higher affinity between enzymes and substrates.

In a possible mechanism of peroxidase activity, which we are here proposing, cerium oxide NSs catalyze the decomposition of H_2O_2 to produce $^{\bullet}OH$ radicals that oxidize the peroxidase substrate represented by TMB. This process is consistent with the observed color change of the solution from blue to yellow.[53] Such a catalytic activity of the proposed nanozyme was demonstrated by monitoring the presence of $^{\bullet}OH$ radicals from this reaction via electron paramagnetic resonance (EPR) spectroscopy. EPR is sensitive to short-living free radicals if spin traps or spin probes that prevent their rapid spin quenching can be used.[54] To identify hydroxyl radicals generated in the catalytic cerium oxide NSs system, EPR was performed by adding DMPO as a spin trap to the solution, and a parametric study was performed, as demonstrated in Figure 5.

The EPR spectrum of DMPO−OH corresponds to line a in Figure 5A. The signal increases at decreasing pH, with increasing amounts of DMPO−$^{\bullet}OH$ adducts being observed at lower pH when the reaction was performed in the presence of a constant amount of cerium oxide NSs. Conversely, no pH dependence of the EPR signal of DMPO was observed when the reaction was performed in the absence of the nanocomposite (Figure 5A, line a), which thus acts as a catalyst for the H_2O_2 decomposition. This model is in agreement with increasing enzyme activity at lower pH because more $^{\bullet}OH$ radicals are produced under acidic conditions. These results confirmed the production of $^{\bullet}OH$ radicals catalyzed by cerium oxide NSs. Furthermore, not only the concentration of generated $^{\bullet}OH$ radicals but also the concentration of the cerium oxide NS catalyst is affected by the pH of the solution. The *g*-values were 2.00553, 2.00548, and 2.00557 at pH values of 11, 7, and 3, respectively, which are close to the values reported in previous studies.[55] The EPR spectrum of DMPO−OH was contaminated by a triplet signal due to the nitrosyl radicals arising from the partial degradation of DMPO trap (black dots).[56] In our measurement, the time between the spin labeling and the measurements was 5−10 min, so the additional hyperfine splitting could not attribute to the superoxide radicals ($^{\bullet}O_2^-$) because it is known that the $^{\bullet}O_2^-$ adduct of DMPO (DMPO−OOH) is unstable (lifetime is 30−90 s) and it spontaneously decays into the DMPO−hydroxyl adduct.[57,58] Furthermore, the reaction rates of DMPO with $^{\bullet}O_2^-$ and $^{\bullet}O_2H$ are extremely smaller compared to that with OH radical. The rate constants of DMPO with $^{\bullet}O_2^-$ and $^{\bullet}O_2H$ are 2−170 and 6.6×10^3 $M^{-1}\cdot s^{-1}$, respectively, while that with $^{\bullet}OH$ is reported to be $1.9–4.3 \times 10^9$ $M^{-1}\cdot s^{-1}$.[59,60] Therefore, the detection of $^{\bullet}O_2-$ with DMPO is not facile. Figure 5B shows that when the nanoparticle concentration is varied from 0 (line a) to 12 mg·mL^{-1} (line d), the catalytic activity also increases, consistent with an increase of the $^{\bullet}OH$ signal up to 8 mg·mL^{-1} cerium oxide (line c) NP and a saturation of the

https://dx.doi.org/10.1021/acsomega.9b03252
ACS Omega 2020, 5, 11883−11894

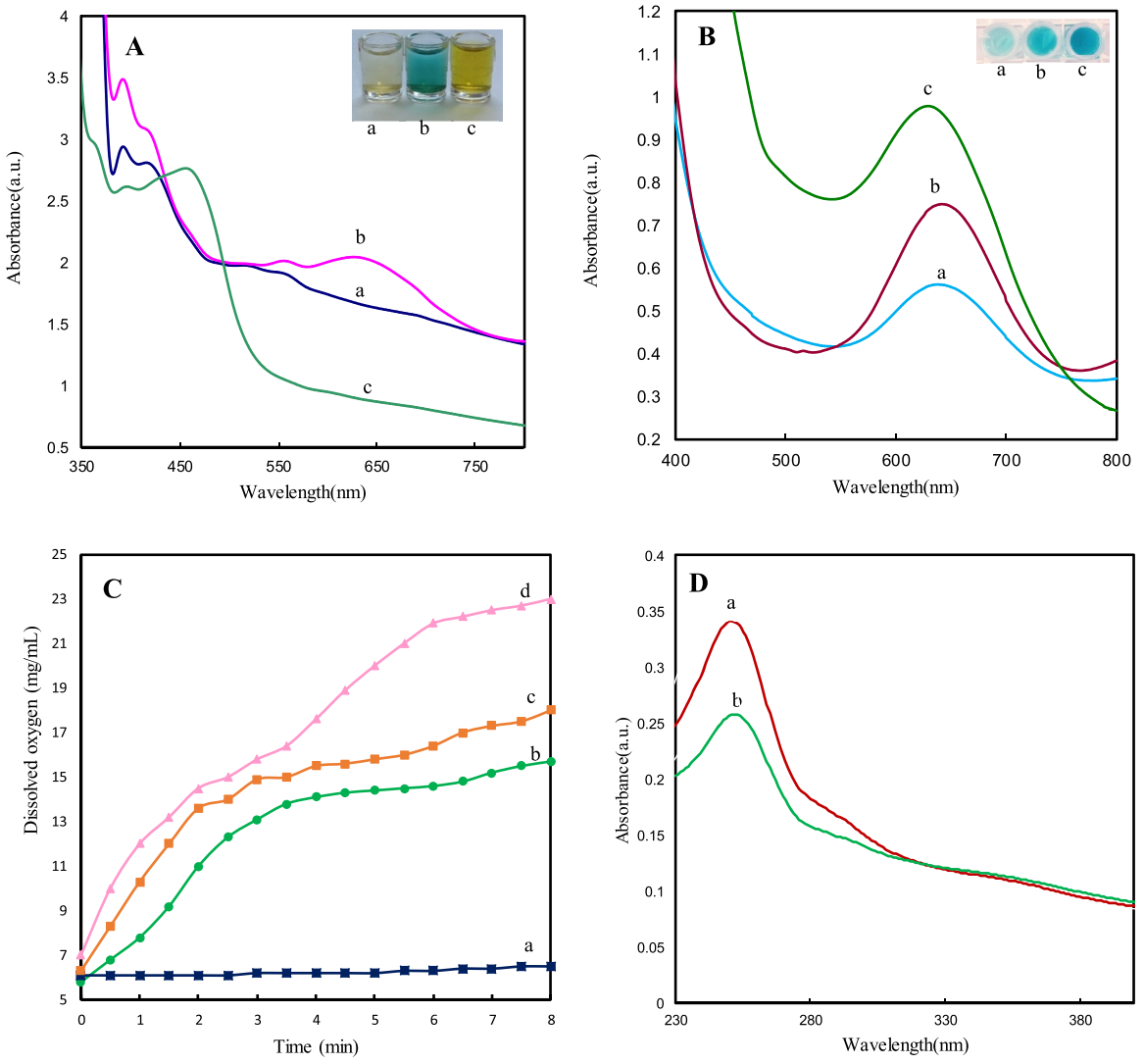

Figure 3. (A) UV−vis spectra and photographs of (a) cerium oxide NSs solution, (b) cerium oxide NSs + TMB + H_2O_2, and (c) cerium oxide NSs + TMB + H_2O_2 + H_2SO_4 (concentration of enzyme: 2 mg·mL^{-1}, reaction time: 5 min). (B) Effect of O_2 concentration on the direct oxidation of TMB by cerium oxide without H_2O_2 ((a) N_2, (b) air, (c) O_2). (C) Dissolved oxygen generation catalyzed by cerium oxide NSs at different concentrations (a) 0 mg·mL^{-1}, (b) 1 mg·mL^{-1}, (c) 2 mg·mL^{-1}, and (d) 4 mg·mL^{-1}. (D) UV−vis spectra of (a) NBT and (b) NBT + cerium oxide NSs + H_2O_2.

effect at higher concentrations. The variation of H_2O_2 concentration from 0% (Figure 5C, line a) to 12% (line d) was also observed to improve the process effectiveness through the addition of more reagents, with an increase in the EPR signal intensity, indicating the generation of more DMPO−$^{\bullet}$OH(aq) adducts.

2.2.2. Oxidase-like Catalytic Activity of Cerium Oxide NSs. The prepared cerium oxide NSs could directly oxidize TMB, leading to blue color products even in the absence of H_2O_2 (Figure 3B). This indicates that cerium oxide NSs also exhibit oxidase-like catalytic activity. To further study the oxidation of the TMB chromogenic substrate by cerium oxide NSs, the effect of the oxidizing agent (dissolved oxygen) in the reaction system was investigated. Compared to bubbling an inert gas into the system of N_2, the absorbance of oxidized TMB at 652 nm was significantly increased after saturation with O_2. It is therefore concluded that increasing the concentration of oxygen as the electron acceptor in the oxidation of TMB can enhance the oxidase-like activity of cerium oxide NSs.

2.2.3. Catalase-like Catalytic Activity of Cerium Oxide NSs. To investigate the catalase-like activity of cerium oxide NSs, the concentration of dissolved oxygen in the system, consisting of cerium oxide NSs and H_2O_2, was recorded using a portable meter. The value of the dissolved oxygen concentration was monitored for 10 min as a function of cerium oxide NS concentration. As shown in Figure 3C, the concentration of dissolved oxygen increased proportionally to the concentration. This indicated that cerium oxide NSs can decompose H_2O_2 into O_2 and provided strong evidence of the catalase-like activity. The production of O_2 was also monitored by EPR by incorporating a spin probe (^{15}N-PDT) in the system. The bimolecular combination of paramagnetic O_2 and N-PDT results in shorter spin−spin relaxation times, broadening the EPR line widths with respect to the pristine EPR signal of the pure spin probe.[61] As shown in Figure 6A, where the pH increased to 11 in the presence of cerium oxide NSs and H_2O_2, the EPR signal line width increased as well, with a consistent signal intensity decrease to account for a constant N-PDT concentration. The EPR line width also broadens with

https://dx.doi.org/10.1021/acsomega.9b03252
ACS Omega 2020, 5, 11883−11894

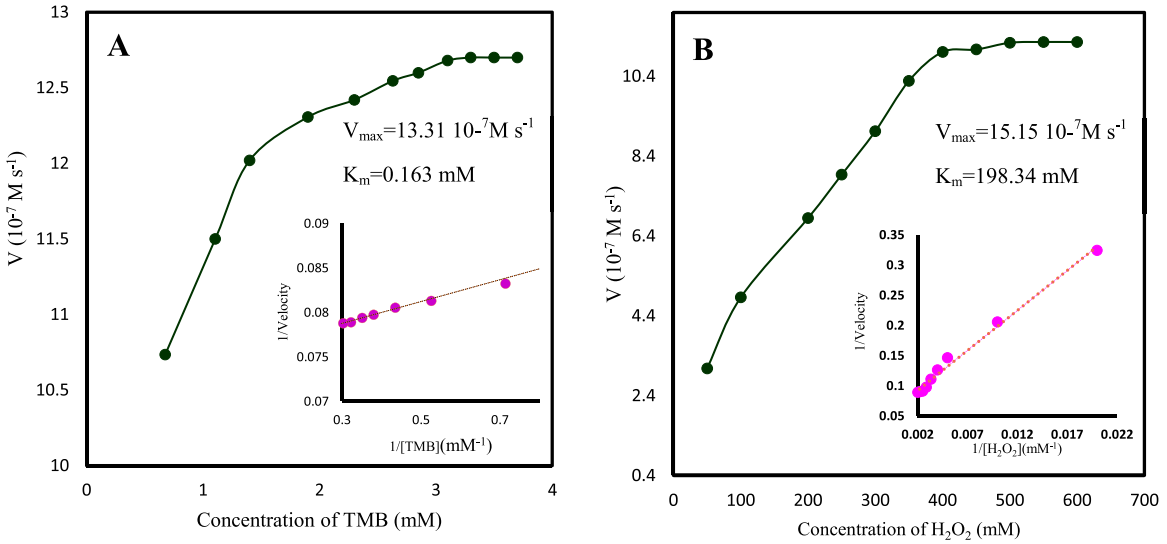

Figure 4. Steady-state kinetic analyses using the Michaelis−Menten model and Lineweaver−Burk model (insets) for cerium oxide NSs by (A) TMB as substrate and (B) H_2O_2 as substrate.

increasing cerium oxide NS concentration (Figure 6B). This also indicates increased oxygen formation due to the stronger catalase-like activity of more concentrated cerium oxide NSs.

2.3. Electrocatalytic Activity of Cerium Oxide NSs. The electrocatalytic activity of cerium oxide NSs was tested by modifying the Au working electrode with cerium oxide NSs. A three-electrode microfluidic chip is used as the electrochemical cell for recording cyclic voltammograms (CV) and determining sensor performance. Cyclic voltammograms (CVs) were recorded for (a) bare Au electrode, (b) cerium oxide NS-modified Au electrode, (c) Au electrode + H_2O_2, and (d) cerium oxide NS-modified Au electrode + H_2O_2 in 0.1 M phosphate-buffered saline (PBS) (pH = 7.4) with a scan rate of 50 mV·s^{-1} (Figure 7A). The bare Au electrode and cerium oxide NS-modified Au electrode did not show any voltammetric response (curves a and b), and upon addition of H_2O_2, a redox process was detected on the Au bare electrode, indicating reduction of H_2O_2 (curve c). However, a large enhancement in the H_2O_2 redox response was observed for the nanoparticle-modified Au electrode (curve d). The oxidation and reduction responses of the electrode-modified cerium oxide NSs when reacting with H_2O_2 clearly show the catalase and peroxidase activities of cerium oxide NSs. The cerium oxide/Au electrode therefore can act as a mimetic catalase, where it significantly electrocatalyzes the decomposition of hydrogen peroxide (H_2O_2) to water (H_2O) and molecular oxygen (O_2) and also acts as a mimetic peroxidase to generate $OH^{\bullet}$ radicals via decomposition of H_2O_2.[30,62]

2.4. Investigation of the Effect of pH on Cerium Oxide/Au Electrode Response. To understand the effect of pH on the electrochemical properties of the cerium oxide/Au electrode in the presence of H_2O_2, electrocatalytic studies were performed at three different pH values: 5.0, 7.0, and 9.0 in the presence of H_2O_2 (10 mM) using a N_2-purged PBS (0.1 M) with a scan rate of 50 mV·s^{-1}, and the results are shown in Figure 7B. At pH = 5.0, both oxidation and reduction were observed; however, the cathodic peak current is higher than the anodic peak, indicating that the peroxidase activity is dominant in cerium oxide NSs at lower pH (curve a). By increasing the buffer solution pH, the cathodic peak current decreases while the anodic peak current is increased relative to curve a, showing dominant catalase activity at higher pH values (curves b and c). These results demonstrate the pH switchability of the catalytic properties of cerium oxide NSs: at acidic pH (pH < 7), the peroxidase catalytic activity is dominant, while at basic pH (pH > 7), the catalase activity is dominant.

2.5. Analytical Performance of Cerium Oxide NS-Modified Au Electrode for Detection of H_2O_2. Figure 7C shows the CVs of cerium oxide NS-modified Au electrode in the presence of different concentrations of H_2O_2. As can be seen, with increasing H_2O_2 concentration, the reduction current increased, demonstrating the excellent catalytic activity of cerium oxide NSs toward the reduction of H_2O_2. Thereupon, the detection sensitivity of cerium oxide NS-modified electrodes to aqueous H_2O_2 was explored through a chronoamperometric study shown in Figure 8. The response for the different amounts of H_2O_2 is shown by the $I-t$ curves collected at −0.5 V in Figure 8A, which indicates that the reduction currents increase gradually with higher concentrations of H_2O_2. The calibration plot indicates good linearity for the reduction current versus H_2O_2 concentrations in the range from 100 to 20 mM (Figure 8A). The linear regression equation generated for cerium oxide NS-modified electrodes was i (μA) = 1.03 log$C$ (μM) + 1.72 μA with a correlation coefficient of R^2 = 0.992 (Figure 8B). The lowest concentration of H_2O_2 that could be estimated by this microfluidic electrochemical sensor was 20 nM (S/N = 3), and the sensitivity was calculated to be 226.4 μA·cm^{-2}·μM^{-1} based on this result. Compared to previously reported H_2O_2 sensors based on other nanomaterials or enzymes, this detection method based on microfluidic device outperforms the sensitivity and detection limit of other sensors, as shown in Table 1. The stability of the microfluidic device was examined after 2 weeks, with the result showing that the current through the device with 1 mM H_2O_2 exhibited only a small deviation over time with a relative standard deviation (RSD) of 3.04%. Six repeated measurements of 1 mM H_2O_2 led to a relative standard deviation of 2.9%, further showing good reproducibility of the biosensing interface. The selectivity of cerium oxide/Au electrode for H_2O_2 detection in PBS was also studied by evaluation of the interference effect of coexisting

https://dx.doi.org/10.1021/acsomega.9b03252
ACS Omega 2020, 5, 11883−11894

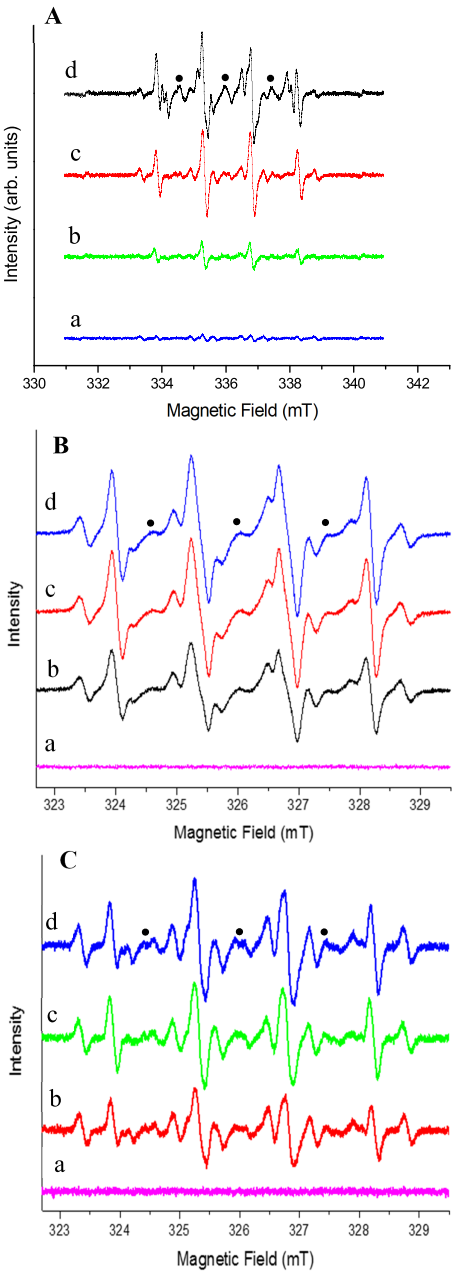

Figure 5. Experimental EPR spectra recorded at room temperature after the reaction of cerium oxide NSs with H_2O_2 in the presence of DMPO spin trap. (The nitroxide degradation product of the spin trap is indicated by black dots.) EPR spectrum of the liquid phase separated from the (A) cerium oxide NSs at varying pH: (a) control (without cerium oxide NSs), (b) pH = 11, (c) pH = 7.0, and (d) pH = 3; (B) various cerium oxide NS concentrations: (a) 0 mg·mL^{-1}, (b) 4 mg·mL^{-1}, (c) 8 mg·mL^{-1}, and (d) 12 mg·mL^{-1}; and (C) various H_2O_2 concentrations: (a) 0%, (b) 4%, (c) 8%, and (d) 12%.

compounds such as ascorbic acid (AA), dopamine (DA), uric acid (UA) glutathione (GSH), and glucose on the electrode response. As illustrated in Figure 8C, there are negligible current responses when interfering molecules were used, confirming the good anti-interference ability of the biomimetic sensor for H_2O_2 detection.

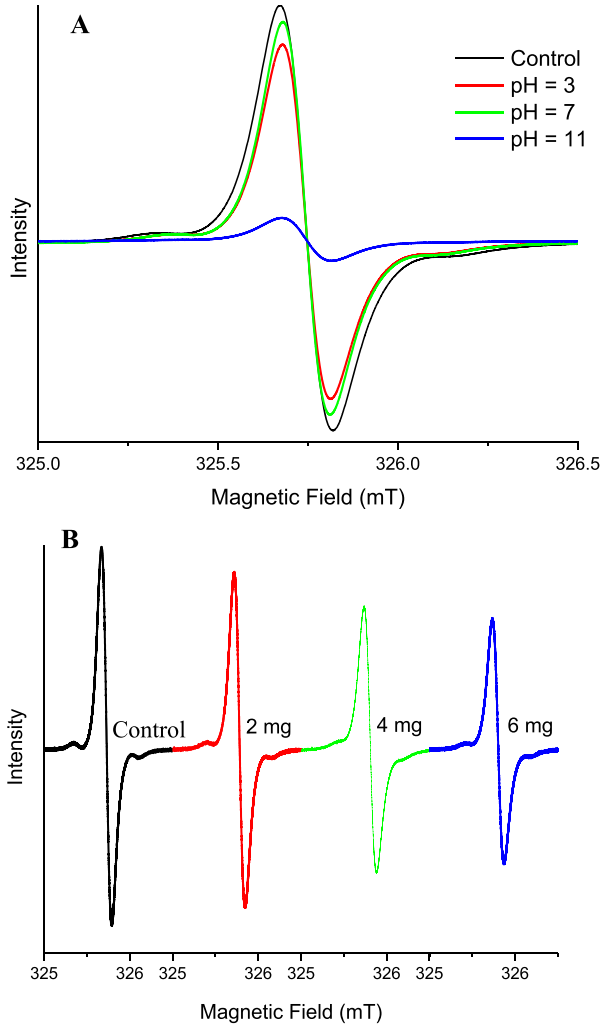

Figure 6. EPR spectra of ^{15}N-PDT (A) in the presence of 2 mg of cerium oxide NSs and H_2O_2 (5%) at different pH values, and (B) in the presence of H_2O_2 (5%) and different concentration of cerium oxide NSs.

2.6. Real-Time Detection of H_2O_2 Released from Living Cells. To investigate the capability of the proposed system for real-time detection of H_2O_2, we chose the PC 12 cell as a model because it can release a trace amount of H_2O_2 under the stimulation of ascorbic acid (AA).[63] The as-prepared 10^6 cells were suspended in 500 μL of PBS (pH = 7.4) for further use. As shown in Figure 8D, in the presence of PC 12 cells, the cathodic current increases to a higher platform after the addition of 4 μM AA (curve c), which corresponds to about 0.1 μM H_2O_2 released from the living cells, confirming that the trace amounts of H_2O_2 released from a living cell can be detected rapidly by the cerium oxide NSs. However, no changes in current are observed in the absence of either cells (curve b) or AA (curve a) under the same conditions, indicating that H_2O_2 is released from cells under the stimulation of AA. These results suggest that the fabricated microfluidic device is highly sensitive and reliable for the detection of H_2O_2 in living cells. So, compared to the advantages such as high activity, low detection limit, wide concentration range, and applicability of the presented sensor for measuring H_2O_2 release from cells, the limitation of the purposed sensor is negligible.

https://dx.doi.org/10.1021/acsomega.9b03252
ACS Omega 2020, 5, 11883−11894

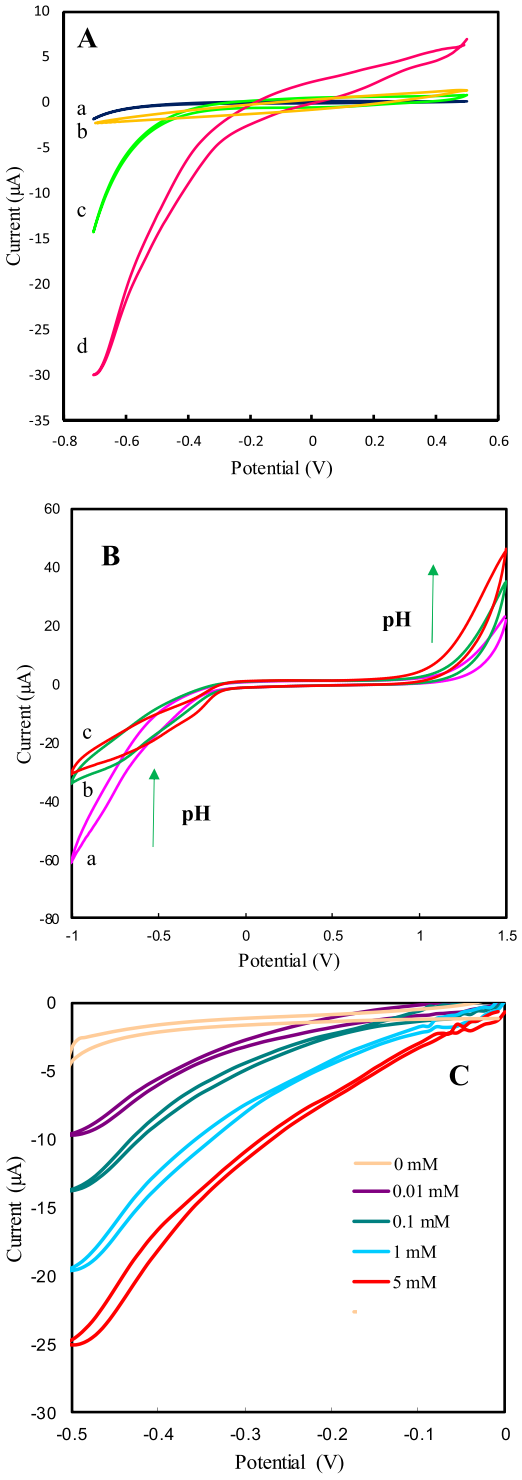

Figure 7. (A) Cyclic voltammograms of (a) bare Au electrode, (b) Au electrode/cerium oxide, (c) Au electrode + H_2O_2, and (d) Au electrode/cerium oxide + H_2O_2. (B) Cyclic voltammograms of Au electrode/cerium oxide + H_2O_2 at different pH values: (a) 5, (b) 7, and (c) 9. (C) Cyclic voltammograms of Au electrode/cerium oxide in the presence of varied H_2O_2 concentrations, recorded in N_2-purged PBS (0.1 M) at a scan rate of 0.03 $V{\cdot}s^{-1}$.

3. CONCLUSIONS

In summary, cerium oxide NSs were synthesized by a facile hydrothermal route and exhibited triple-enzyme mimetic activity: oxidase-, peroxidase-, and catalase-like activities. The enzyme mimic properties of cerium oxide NSs can be modulated by adjusting the pH. The peroxidase-like activity is predominant under acidic pH, while the catalase-like activity is prevalent under alkaline conditions. The underlying mechanisms of the catalytic processes involving cerium oxide NSs were investigated by means of EPR spectroscopy, which revealed that the peroxidase-like activity originates from the ability to produce hydroxyl ($^{\bullet}OH$) radicals. The catalase-like activity causes the decomposition of H_2O_2 to O_2. The as-prepared nanocomposite was used for the electrochemical detection of H_2O_2 using LOC microfluidic devices. The chronoamperometric technique was utilized for the sensitive detection of H_2O_2. The linear range of this method was found to be between 100 nM and 20 mM, with a detection limit of 20 nM. The methods we developed have decisive advantages in terms of wide linear range, low detection limit, high sensitivity, easiness of operation, and good practicability. The developed methods were applied to the detection of H_2O_2 in living cells, which may be competitive with existing methods because of their low cost, simplicity, and reproducibility. We believe that our microfluidic sensors, along with electrochemical detection, may contribute to the growth of biosensing technologies toward practical applications in bioanalysis, food safety, and environmental diagnostics.

4. EXPERIMENTAL SECTION

4.1. Materials and Instruments. Cerium nitrate hexahydrate $Ce(NO_3)_3{\cdot}6H_2O$, terephthalic acid $C_6H_4(CO_2H)_2$, urea $(CO(NH_2)_2)$, H_2O_2, 3,3′,5,5 tetramethylbenzidine (TMB), glucose, dopamine, uric acid, glutathione, and ascorbic acid and all other reagents were purchased from Merck or Fluka. All chemicals and reagents were of analytical grade and directly used without further purification. Deionized water produced from a Milli-Q Plus system (Millipore) was used in all experiments.

Scanning electron microscopy (SEM) and transmission electron microscopy (TEM) images were obtained with a MIRA3 TESCAN HV: 20.0 kV instrument and a Philips EM 280 microscope, respectively. XRD patterns were recorded on a Bruker D8 Advance diffractometer equipped with a copper source and a general area detector diffraction system (GADDS). The FTIR and UV−vis spectra were recorded by a Vector-22 Bruker spectrophotometer and a SPECTROD 250-Analytik Jena spectrophotometer, respectively. Dissolved oxygen was monitored after the addition of H_2O_2 by a Handheld meter Oxi 330i/340i (WTW GmbH & Co. KG).

Electron paramagnetic resonance measurements were performed using a Jeol FA-200 EPR spectrometer operating in the X-band at 9.1 MHz and equipped with a cylindrical resonator. The hydroxyl radicals generated in the liquid phase were detected by applying the spin trapping technique. 5,5-Dimethyl-1-pyrroline *N*-oxide (DMPO) with a concentration of 20 mM was chosen as a suitable spin trap because of its high trapping ability and selectivity toward oxygen-centered radicals. In the spin trapping experiments, a predetermined amount of cerium oxide NSs was contacted with a mixture of 1 mL of H_2O_2/H_2O and 10 μL of DMPO. The liquid sample (5 μL) was inserted into a quartz capillary tube with 1.0 mm inner diameter using a micropipette. The filled capillary was then sealed with parafilm and placed in a quartz glass EPR tube of 5 mm inner diameter (Wilmad LabGlass, 710-SQ-250M) and inserted in the microwave cavity, with all measurements recorded at room temperature unless otherwise stated.[56]

https://dx.doi.org/10.1021/acsomega.9b03252
ACS Omega 2020, 5, 11883−11894

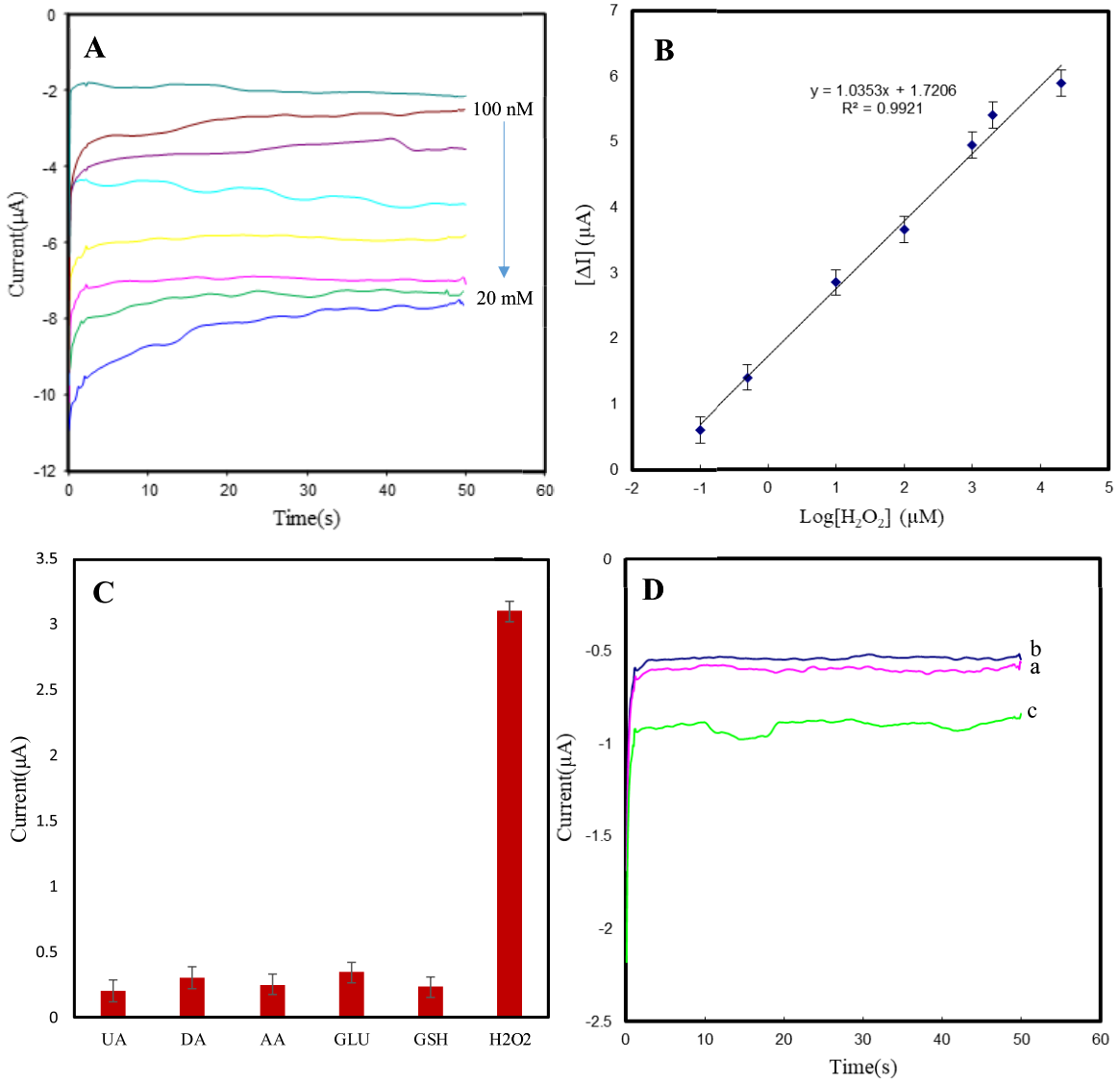

Figure 8. (A) Chronoamperometric responses of Au electrode/cerium oxide upon addition of different H_2O_2 concentrations. Applied potential: −0.5 V. (B) Logarithmic relationship between the concentrations of H_2O_2 (0.1, 0.5, 10, 100, 1000, 2000, and 20 000 μM). (C) Interference studies of cerium oxide-based lab-on-a-chip device on addition of 1 mM UA, DA, AA, GLU, GSH and 0.2 mM H_2O_2. (D) Chronoamperometric responses of Au electrode/cerium oxide for the reduction of H_2O_2 released from 10^6 PC 12 cells in 1 mL of 1 × PBS (pH = 7.4): (a) PC12 cells, (b) AA (4 μM), and (c) PC12 cells upon injection of 4 μM AA.

Table 1. Comparison of the Performance of Various Hydrogen Peroxide Sensors

electrode materials	linear range (μM)	detection limit (μM)	refs
MnO_2 nanosheets	up to 454	0.005	63
graphene/Pt nanocomposite	0.5−3475	0.2	64
Se/Pt nanocomposites	10−15 000	3.1	65
RGO−Au−PTBO	5.0−25 362	0.2	66
rGO@CeO_2-AgNPs	0.5−12 000	0.21	67
TiO_2@Cu_2O	1−15 mM	0.15	68
Au/GS/HRP/CS	5−5130	1.7	69
cerium oxide NSs	0.1−20 000	0.01	this work

4.2. Synthesis of Cerium Oxide NSs. Cerium oxide NSs were prepared by a wet-chemical deposition precipitation method. Briefly, 0.25 g of $Ce(NO_3)_3{\cdot}6H_2O$ was dissolved in 10 mL of distilled water. Subsequently, 0.02 g of urea was added to the solution under vigorous stirring. Then, 10 mL of terephthalic acid solution (60 μM) was added to the reaction solution. After stirring for 15 min, the precipitate product was transferred to a 40 mL Teflon-lined stainless steel autoclave and kept in an electric oven at 150 °C for 6 h. The autoclave was then taken out from the oven and left to cool to room temperature. The produced precipitate was collected via centrifugation, washed thoroughly with water and ethanol, and dried at 60 °C overnight.

4.3. Fabrication of Electrochemical Microfluidic Devices. All experiments were carried out in microfluidic chips made of polydimethylsiloxane (PDMS). The fabrication process can be broken down into three major steps: (1) fabrication of a three-electrode setup, (2) casting of PDMS, and (3) plasma bonding of PDMS over the prepared electrodes on the glass substrate. The electrochemical cell for detection comprised a set of three electrodes: a counter electrode (CE), a working electrode (WE), and a reference

https://dx.doi.org/10.1021/acsomega.9b03252
ACS Omega 2020, 5, 11883−11894

electrode (RE). Gold (Au) was chosen as the material for electrodes, and the electrochemical device was fabricated using standard photolithography techniques. The modified electrode was fabricated by drop-casting 5 μL of aqueous cerium oxide NSs (1 mg·mL^{-1}) solution on the cleaned Au working electrode. For fabrication of microfluidic channels, a mixture of polydimethylsiloxane (PDMS) prepolymer and curing agent (10:1) was poured onto the preetched silicon mold followed by curing at 80 °C for 12 h. Then, the cured PDMS was peeled off and placed on the clean bare glass substrate. The width and depth of the channel were both 200 μm, and the surface area of the working electrode was 0.2 mm^2. For better adhesion of PDMS channel to the glass, the sample was annealed at 80 °C for 2 h. Finally, it was treated with oxygen plasma before it was bonded to the patterned glass substrate. To ensure strong bonding between the PDMS channel and the glass substrate, the device was sandwiched between two plexiglass sheets. The width and depth of the channel were both 200 μm.

4.4. Electrochemical H_2O_2 Analysis by Microfluidic Electrochemical Devices. All electrochemical experiments were performed with a computer-controlled potentiostat, Autolab electrochemical analyzer model PGSTAT30 (Eco Chemie, Utrecht, the Netherlands) driven with GPES software (Eco Chemie) in conjunction with a personal computer for data storage and processing. A three Au electrode configuration was applied, in which the cerium oxide NS-modified Au electrode was used as the working electrode (WE) and placed into a microfluidic device. Peristaltic pumps (ISM834C) were connected to the inlet of the microfluidic device to injection of solution into the chip. The electrochemical sensing of H_2O_2 was carried out in 0.1 M PBS (pH = 7.4), and the PBS was degassed with N_2 for 20 min before test. Cyclic voltammetric measurements for hydrogen peroxide were performed at a scanning rate of 50 mV·s^{-1}. Chronoamperometry was performed at a constant applied potential of −0.5 V, and the resulting chronoamperograms were subjected to baseline correction before further analysis.

4.5. Detection of H_2O_2 in Real Sample. PC 12 cells were cultured in Dulbecco's modified Eagle's medium (DMEM) solution containing 1% penicillin, 1% streptomycin, and 10% fetal bovine serum in a humidified atmosphere of 5% CO_2 for 24 h at 37 °C in culture dishes. Then, the cells were removed from the Petri dish by trypsinization and washed three times with sterile buffer, followed by suspension in fresh DMEM. Upon the addition of AA (4 μM), the chronoamperometric current response flux of H_2O_2 in about 10^6 cells was recorded.

AUTHOR INFORMATION

Corresponding Author

Abdollah Salimi − *Department of Chemistry and Research Center for Nanotechnology, University of Kurdistan, 66177-15175 Sanandaj, Iran; Department of Chemistry, University of Western Ontario, N6A 5B7 London, Ontario, Canada;* orcid.org/0000-0003-1137-1854; Email: absalimi@uok.ac.ir, absalimi@yahoo.com

Authors

Negar Alizadeh − *Department of Chemistry, University of Kurdistan, 66177-15175 Sanandaj, Iran*

Tsun-Kong Sham − *Department of Chemistry, University of Western Ontario, N6A 5B7 London, Ontario, Canada;* orcid.org/0000-0003-1928-6697

Paul Bazylewski − *Department of Physics and Astronomy, University of Western Ontario, N6A 3K7 London, Canada*

Giovanni Fanchini − *Department of Physics and Astronomy, University of Western Ontario, N6A 3K7 London, Canada;* orcid.org/0000-0002-2502-7475

Complete contact information is available at: https://pubs.acs.org/10.1021/acsomega.9b03252

Notes

The authors declare no competing financial interest.

ACKNOWLEDGMENTS

The authors acknowledge financial support from the Research Office of University of Kurdistan (grant number 4.1261) and Iranian Nanotechnology Initiative Funds for research on microfluidic-based sensors.

REFERENCES

(1) Gao, L.; Zhuang, J.; Nie, L.; Zhang, J.; Zhang, Y.; Gu, N.; Wang, T.; Feng, J.; Yang, D.; Perrett, S.; Yan, X. Intrinsic peroxidase-like activity of ferromagnetic nanoparticles. *Nat. Nanotechnol.* **2007**, *2*, 577.

(2) Nakamura, E.; Isobe, H. Functionalized fullerenes in water. The first 10 years of their chemistry, biology, and nanoscience. *Acc. Chem. Res.* **2003**, *36*, 807−815.

(3) Xiong, Y.; Chen, S.; Ye, F.; Su, L.; Zhang, C.; Shen, S.; Zhao, S. Synthesis of a mixed valence state Ce-MOF as an oxidase mimetic for the colorimetric detection of biothiols. *Chem. Commun.* **2015**, *51*, 4635−4638.

(4) Asati, A.; Kaittanis, C.; Santra, S.; Perez, J. M. pH-tunable oxidase-like activity of cerium oxide nanoparticles achieving sensitive fluorigenic detection of cancer biomarkers at neutral pH. *Anal. Chem.* **2011**, *83*, 2547−2553.

(5) Alizadeh, N.; Salimi, A.; Hallaj, R.; Fathi, F.; Soleimani, F. CuO/WO_3 nanoparticles decorated graphene oxide nanosheets with enhanced peroxidase-like activity for electrochemical cancer cell detection and targeted therapeutics. *Mater. Sci. Eng., C* **2019**, *99*, 1374−1383.

(6) Ding, Y.; Yang, B.; Liu, H.; Liu, Z.; Zhang, X.; Zheng, X.; Liu, Q. FePt-Au ternary metallic nanoparticles with the enhanced peroxidase-like activity for ultrafast colorimetric detection of H_2O_2. *Sens. Actuators, B* **2018**, *259*, 775−783.

(7) Jain, S.; Panigrahi, A.; Sarma, T. K. Counter Anion-Directed Growth of Iron Oxide Nanorods in a Polyol Medium with Efficient Peroxidase-Mimicking Activity for Degradation of Dyes in Contaminated Water. *ACS Omega* **2019**, *4*, 13153−13164.

(8) Liu, C. P.; Wu, T. H.; Liu, C. Y.; Chen, K. C.; Chen, Y. X.; Chen, G. S.; Lin, S. Y. Self-Supplying O_2 through the Catalase-Like Activity of Gold Nanoclusters for Photodynamic Therapy against Hypoxic Cancer Cells. *Small* **2017**, *13*, No. 1700278.

(9) Yamada, M.; Yoshinari, N.; Kuwamura, N.; Saito, T.; Okada, S.; Maddala, S. P.; Harano, K.; Nakamura, E.; Yamagami, K.; Yamanaka, K.; et al. Heterogeneous catalase-like activity of gold (I)−cobalt (III) metallosupramolecular ionic crystals. *Chem. Sci.* **2017**, *8*, 2671−2676.

(10) Mu, J.; Zhao, X.; Li, J.; Yang, E.-C.; Zhao, X.-J. Novel hierarchical NiO nanoflowers exhibiting intrinsic superoxide dismutase-like activity. *J. Mater. Chem. B* **2016**, *4*, 5217−5221.

(11) Singh, O.; Tyagi, N.; Olmstead, M. M.; Ghosh, K. The design of synthetic superoxide dismutase mimetics: seven-coordinate water soluble manganese (II) and iron (II) complexes and their superoxide dismutase-like activity studies. *Dalton Trans.* **2017**, *46*, 14186−14191.

(12) Lin, Y.; Ren, J.; Qu, X. Catalytically active nanomaterials: a promising candidate for artificial enzymes. *Acc. Chem. Res.* **2014**, *47*, 1097−1105.

(13) Wei, H.; Wang, E. Nanomaterials with enzyme-like characteristics (nanozymes): next-generation artificial enzymes. *Chem. Soc. Rev.* **2013**, *42*, 6060−6093.

(14) Wang, Q.; Zhang, X.; Huang, L.; Zhang, Z.; Dong, S. One-pot synthesis of Fe_3O_4 nanoparticle loaded 3D porous graphene nanocomposites with enhanced nanozyme activity for glucose detection. *ACS Appl. Mater. Interfaces* **2017**, *9*, 7465−7471.
(15) Zhao, J.; Dong, W.; Zhang, X.; Chai, H.; Huang, Y. FeNPs@ Co_3O_4 hollow nanocages hybrids as effective peroxidase mimics for glucose biosensing. *Sens. Actuators, B* **2018**, *263*, 575−584.
(16) Dong, W.; Zhuang, Y.; Li, S.; Zhang, X.; Chai, H.; Huang, Y. High peroxidase-like activity of metallic cobalt nanoparticles encapsulated in metal−organic frameworks derived carbon for biosensing. *Sens. Actuators, B* **2018**, *255*, 2050−2057.
(17) Wang, C.; Liu, C.; Luo, J.; Tian, Y.; Zhou, N. Direct electrochemical detection of kanamycin based on peroxidase-like activity of gold nanoparticles. *Anal. Chim. Acta* **2016**, *936*, 75−82.
(18) Dong, J.; Song, L.; Yin, J.-J.; He, W.; Wu, Y.; Gu, N.; Zhang, Y. Co_3O_4 nanoparticles with multi-enzyme activities and their application in immunohistochemical assay. *ACS Appl. Mater. Interfaces* **2014**, *6*, 1959−1970.
(19) Li, J.; Liu, W.; Wu, X.; Gao, X. Mechanism of pH-switchable peroxidase and catalase-like activities of gold, silver, platinum and palladium. *Biomaterials* **2015**, *48*, 37−44.
(20) Mu, J.; Wang, Y.; Zhao, M.; Zhang, L. Intrinsic peroxidase-like activity and catalase-like activity of Co_3O_4 nanoparticles. *Chem. Commun.* **2012**, *48*, 2540−2542.
(21) Wang, Q.; Zhang, L.; Shang, C.; Zhang, Z.; Dong, S. Triple-enzyme mimetic activity of nickel−palladium hollow nanoparticles and their application in colorimetric biosensing of glucose. *Chem. Commun.* **2016**, *52*, 5410−5413.
(22) Ding, Y.; Wang, G.; Sun, F.; Lin, Y. Heterogeneous Nanostructure Design Based on the Epitaxial Growth of Spongy MoS x on 2D Co (OH) $_2$ Nanoflakes for Triple-Enzyme Mimetic Activity: Experimental and Density Functional Theory Studies on the Dramatic Activation Mechanism. *ACS Appl. Mater. Interfaces* **2018**, *10*, 32567−32578.
(23) Li, H.; Wang, T.; Wang, Y.; Wang, S.; Su, P.; Yang, Y. Intrinsic triple-enzyme mimetic activity of V_6O_{13} nanotextiles: mechanism investigation and colorimetric and fluorescent detections. *Ind. Eng. Chem. Res.* **2018**, *57*, 2416−2425.
(24) Alizadeh, N.; Salimi, A.; Hallaj, R. Mimicking peroxidase activity of Co_2 (OH) $_2CO_3$-CeO_2 nanocomposite for smartphone based detection of tumor marker using paper-based microfluidic immunodevice. *Talanta* **2018**, *189*, 100−110.
(25) Li, C.; Shi, X.; Shen, Q.; Guo, C.; Hou, Z.; Zhang, J. Hot Topics and Challenges of Regenerative Nanoceria in Application of Antioxidant Therapy. *J. Nanomater.* **2018**, *2018*, No. 4857461.
(26) Wu, J.; Wang, X.; Wang, Q.; Lou, Z.; Li, S.; Zhu, Y.; Qin, L.; Wei, H. Nanomaterials with enzyme-like characteristics (nanozymes): next-generation artificial enzymes (II). *Chem. Soc. Rev.* **2019**, *48*, 1004−1076.
(27) Alizadeh, N.; Salimi, A.; Hallaj, R. Mimicking peroxidase-like activity of Co_3O_4-CeO_2 nanosheets integrated paper-based analytical devices for detection of glucose with smartphone. *Sens. Actuators, B* **2019**, *288*, 44−52.
(28) Ding, H.; Yang, J.; Ma, S.; Yigit, N.; Xu, J.; Rupprechter, G.; Wang, J. Large Dimensional CeO2 Nanoflakes by Microwave-Assisted Synthesis: Lamellar Nano-Channels and Surface Oxygen Vacancies Promote Catalytic Activity. *ChemCatChem* **2018**, *10*, 4100−4108.
(29) Huang, Y.; Long, B.; Tang, M.; Rui, Z.; Balogun, M.-S.; Tong, Y.; Ji, H. Bifunctional catalytic material: An ultrastable and high-performance surface defect CeO_2 nanosheets for formaldehyde thermal oxidation and photocatalytic oxidation. *Appl. Catal., B* **2016**, *181*, 779−787.
(30) Singh, S.; Singh, M.; Mitra, K.; Singh, R.; Gupta, S. K. S.; Tiwari, I.; Ray, B. Electrochemical sensing of hydrogen peroxide using brominated graphene as mimetic catalase. *Electrochim. Acta* **2017**, *258*, 1435−1444.
(31) Vilian, A. T. E.; Chen, S.-M.; Lou, B.-S. A simple strategy for the immobilization of catalase on multi-walled carbon nanotube/poly (L-lysine) biocomposite for the detection of H_2O_2 and iodate. *Biosens. Bioelectron.* **2014**, *61*, 639−647.
(32) Chen, S.; Yuan, R.; Chai, Y.; Hu, F. Electrochemical sensing of hydrogen peroxide using metal nanoparticles: a review. *Microchim. Acta* **2013**, *180*, 15−32.
(33) Chen, W.; Cai, S.; Ren, Q.-Q.; Wen, W.; Zhao, Y.-D. Recent advances in electrochemical sensing for hydrogen peroxide: a review. *Analyst* **2012**, *137*, 49−58.
(34) Watt, B. E.; Proudfoot, A. T.; Vale, J. A. Hydrogen peroxide poisoning. *Toxicol. Rev.* **2004**, *23*, 51−57.
(35) Hong, J.; Maguhn, J.; Freitag, D.; Kettrup, A. Determination of H_2O_2 and organic peroxides by high-performance liquid chromatography with post-column UV irradiation, derivatization and fluorescence detection. *Fresenius' J. Anal. Chem.* **1998**, *361*, 124−128.
(36) Lebiga, E.; Fernandez, R. E.; Beskok, A. Confined chemiluminescence detection of nanomolar levels of H $_2$ O $_2$ in a paper−plastic disposable microfluidic device using a smartphone. *Analyst* **2015**, *140*, 5006−5011.
(37) Chen, S.; Hai, X.; Chen, X.-W.; Wang, J.-H. In situ growth of silver nanoparticles on graphene quantum dots for ultrasensitive colorimetric detection of H_2O_2 and glucose. *Anal. Chem.* **2014**, *86*, 6689−6694.
(38) Yuan, J.; Cen, Y.; Kong, X.-J.; Wu, S.; Liu, C.-L.; Yu, R.-Q.; Chu, X. MnO_2-nanosheet-modified upconversion nanosystem for sensitive turn-on fluorescence detection of H_2O_2 and glucose in blood. *ACS Appl. Mater. Interfaces* **2015**, *7*, 10548−10555.
(39) Teymourian, H.; Salimi, A.; Khezrian, S. Fe_3O_4 magnetic nanoparticles/reduced graphene oxide nanosheets as a novel electrochemical and bioeletrochemical sensing platform. *Biosens. Bioelectron.* **2013**, *49*, 1−8.
(40) Salimi, A.; Hallaj, R.; Soltanian, S.; Mamkhezri, H. Nanomolar detection of hydrogen peroxide on glassy carbon electrode modified with electrodeposited cobalt oxide nanoparticles. *Anal. Chim. Acta* **2007**, *594*, 24−31.
(41) Yamada, K.; Henares, T. G.; Suzuki, K.; Citterio, D. Paper-based inkjet-printed microfluidic analytical devices. *Angew. Chem.* **2015**, *54*, 5294−5310.
(42) Alizadeh, N.; Ghasemi, F.; Salimi, A.; Hallaj, R.; Fathi, F.; Soleimani, F. Polymer nanocomposite film for dual colorimetric and fluorescent ascorbic acid detection integrated single-cell bioimaging with droplet microfluidic platform. *Dyes Pigm.* **2020**, *173*, No. 107875.
(43) Alizadeh, N.; Salimi, A. Polymer dots as a novel probe for fluorescence sensing of dopamine and imaging in single living cell using droplet microfluidic platform. *Anal. Chim. Acta* **2019**, *1091*, 40−49.
(44) Ben-Yoav, H.; Dykstra, P. H.; Bentley, W. E.; Ghodssi, R. A controlled microfluidic electrochemical lab-on-a-chip for label-free diffusion-restricted DNA hybridization analysis. *Biosens. Bioelectron.* **2015**, *64*, 579−585.
(45) Riahi, R.; Shaegh, S. A. M.; Ghaderi, M.; Zhang, Y. S.; Shin, S. R.; Aleman, J.; Massa, S.; Kim, D.; Dokmeci, M. R.; Khademhosseini, A. Automated microfluidic platform of bead-based electrochemical immunosensor integrated with bioreactor for continual monitoring of cell secreted biomarkers. *Sci. Rep.* **2016**, *6*, No. 24598.
(46) Jampaiah, D.; Reddy, T. S.; Kandjani, A. E.; Selvakannan, P.; Sabri, Y. M.; Coyle, V. E.; Shukla, R.; Bhargava, S. K. Fe-doped CeO_2 nanorods for enhanced peroxidase-like activity and their application towards glucose detection. *J. Mater. Chem. B* **2016**, *4*, 3874−3885.
(47) Cho, Y. J.; Jang, H.; Lee, K.-S.; Kim, D. R. Direct growth of cerium oxide nanorods on diverse substrates for superhydrophobicity and corrosion resistance. *Appl. Surf. Sci.* **2015**, *340*, 96−101.
(48) Ikuma, Y.; Oosawa, H.; Shimada, E.; Kamiya, M. Effect of microwave radiation on the formation of Ce_2O (CO_3) $_2$· H_2O in aqueous solution. *Solid State Ionics* **2002**, *151*, 347−352.
(49) Heidari, F.; Irankhah, A. Effect of surfactants and digestion time on nano crystalline cerium oxide characteristics synthesized by differential precipitation. *Ceram. Int.* **2014**, *40*, 12655−12660.
(50) Lin, Z.; Waller, G.; Liu, Y.; Liu, M.; Wong, C. P. Facile synthesis of nitrogen-doped graphene via pyrolysis of graphene oxide

and urea, and its electrocatalytic activity toward the oxygen-reduction reaction. *Adv. Energy Mater.* **2012**, *2*, 884−888.
(51) Varaprasad, K.; Pariguana, M.; Raghavendra, G. M.; Jayaramudu, T.; Sadiku, E. R. Development of biodegradable metaloxide/polymer nanocomposite films based on poly-ε-caprolactone and terephthalic acid. *Mater. Sci. Eng., C* **2017**, *70*, 85−93.
(52) Cui, L.; Wu, J.; Li, J.; Ju, H. Electrochemical sensor for lead cation sensitized with a DNA functionalized porphyrinic metal−organic framework. *Anal. Chem.* **2015**, *87*, 10635−10641.
(53) Su, L.; Qin, W.; Zhang, H.; Rahman, Z. U.; Ren, C.; Ma, S.; Chen, X. The peroxidase/catalase-like activities of MFe_2O_4 (M = Mg, Ni, Cu) MNPs and their application in colorimetric biosensing of glucose. *Biosens. Bioelectron.* **2015**, *63*, 384−391.
(54) Iravani, S.; Soofi, G. J. Measurement of Oxidative Stress Using ESR Spectroscopy. In *Electron Spin Resonance Spectroscopy in Medicine*; Springer, 2019; pp 73−81.
(55) Kurake, N.; Tanaka, H.; Ishikawa, K.; Takeda, K.; Hashizume, H.; Nakamura, K.; Kajiyama, H.; Kondo, T.; Kikkawa, F.; Mizuno, M.; Hori, M. Effects of $^{\bullet}OH$ and $^{\bullet}NO$ radicals in the aqueous phase on H_2O_2 and generated in plasma-activated medium. *J. Phys. D: Appl. Phys.* **2017**, *50*, No. 155202.
(56) Sobańska, K.; Pietrzyk, P.; Sojka, Z. Generation of reactive oxygen species via electroprotic interaction of H_2O_2 with ZrO_2 gel: ionic sponge effect and pH-switchable peroxidase-and catalase-like activity. *ACS Catal.* **2017**, *7*, 2935−2947.
(57) Finkelstein, E.; Rosen, G. M.; Rauckman, E. J. Spin trapping of superoxide and hydroxyl radical: Practical aspects. *Arch. Biochem. Biophys.* **1980**, *200*, 1−16.
(58) Buxton, G. V.; Greenstock, C. L.; Helman, W. P.; Ross, A. B. Critical review of rate constants for reactions of hydrated electrons, hydrogen atoms and hydroxyl radicals ($^{\bullet}OH/^{\bullet}O^{-}$) in aqueous solution. *J. Phys. Chem. Ref. Data* **1988**, *17*, 513−886.
(59) Buettner, G. R.; Oberley, L. W. Considerations in the spin trapping of superoxide and hydroxyl radical in aqueous systems using 5,5-dimethyl-1-pyrroline-1-oxide. *Biochem. Biophys. Res. Commun.* **1978**, *83*, 69−74.
(60) Hawkins, C. L.; Davies, M. J. Detection and characterization of radicals in biological materials using EPR methodology. *Biochim. Biophys. Acta, Gen. Subj.* **2014**, *1840*, 708−721.
(61) Wen, T.; He, W.; Chong, Y.; Liu, Y.; Yin, J.-J.; Wu, X. Exploring environment-dependent effects of Pd nanostructures on reactive oxygen species (ROS) using electron spin resonance (ESR) technique: implications for biomedical applications. *Phys. Chem. Chem. Phys.* **2015**, *17*, 24937−24943.
(62) Alizadeh, N.; Salimi, A.; Hallaj, R.; Fathi, F.; Soleimani, F. Ni-hemin metal−organic framework with highly efficient peroxidase catalytic activity: toward colorimetric cancer cell detection and targeted therapeutics. *J. Nanobiotechnol.* **2018**, *16*, No. 93.
(63) Shu, Y.; Xu, J.; Chen, J.; Xu, Q.; Xiao, X.; Jin, D.; Pang, H.; Hu, X. Ultrasensitive electrochemical detection of H_2O_2 in living cells based on ultrathin MnO_2 nanosheets. *Sens. Actuators, B* **2017**, *252*, 72−78.
(64) Zhang, Y.; Bai, X.; Wang, X.; Shiu, K.-K.; Zhu, Y.; Jiang, H. Highly sensitive graphene−Pt nanocomposites amperometric biosensor and its application in living cell H_2O_2 detection. *Anal. Chem.* **2014**, *86*, 9459−9465.
(65) Li, Y.; Zhang, J.-J.; Xuan, J.; Jiang, L.-P.; Zhu, J.-J. Fabrication of a novel nonenzymatic hydrogen peroxide sensor based on Se/Pt nanocomposites. *Electrochem. Commun.* **2010**, *12*, 777−780.
(66) Chang, H.; Wang, X.; Shiu, K.-K.; Zhu, Y.; Wang, J.; Li, Q.; Chen, B.; Jiang, H. Layer-by-layer assembly of graphene, Au and poly (toluidine blue O) films sensor for evaluation of oxidative stress of tumor cells elicited by hydrogen peroxide. *Biosens. Bioelectron.* **2013**, *41*, 789−794.
(67) Yao, Z.; Yang, X.; Wu, F.; Wu, W.; Wu, F. Synthesis of differently sized silver nanoparticles on a screen-printed electrode sensitized with a nanocomposites consisting of reduced graphene oxide and cerium (IV) oxide for nonenzymatic sensing of hydrogen peroxide. *Microchim. Acta* **2016**, *183*, 2799−2806.
(68) Li, Z.; Xin, Y.; Zhang, Z. New photocathodic analysis platform with quasi-core/shell-structured TiO_2@ Cu_2O for sensitive detection of H_2O_2 release from living cells. *Anal. Chem.* **2015**, *87*, 10491−10497.
(69) Zhou, K.; Zhu, Y.; Yang, X.; Luo, J.; Li, C.; Luan, S. A novel hydrogen peroxide biosensor based on Au−graphene−HRP−chitosan biocomposites. *Electrochim. Acta* **2010**, *55*, 3055−3060.

https://dx.doi.org/10.1021/acsomega.9b03252
ACS Omega 2020, 5, 11883−11894